Soft Matter

www.rsc.org/softmatter

Volume 9 | Number 24 | 28 June 2013 | Pages 5659–5830

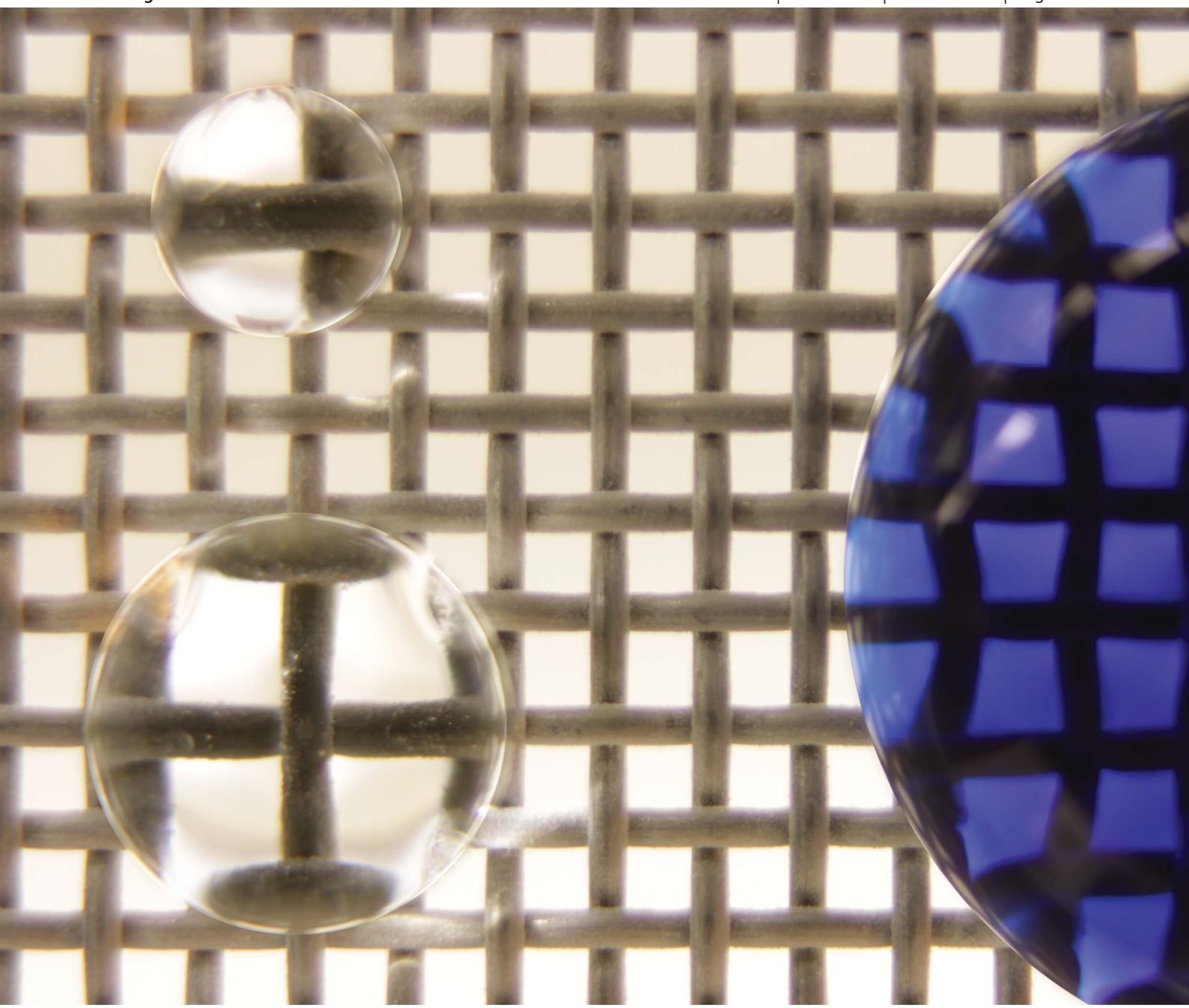

ISSN 1744-683X

RSC Publishing

PAPER

Robert E. Cohen, Gareth H. McKinley *et al.*

Drag reduction for viscous laminar flow on spray-coated non-wetting surfaces

1744-683X(2013)9:24;1-4

Soft Matter

RSC Publishing

PAPER

View Article Online
View Journal | View Issue

Cite this: *Soft Matter*, 2013, **9**, 5691

Drag reduction for viscous laminar flow on spray-coated non-wetting surfaces†

Siddarth Srinivasan,[a] Wonjae Choi,[b] Kyoo-Chul Park,[c] Shreerang S. Chhatre,[a] Robert E. Cohen*[a] and Gareth H. McKinley*[c]

We estimate the effective Navier-slip length for flow over a spray-fabricated liquid-repellent surface which supports a composite solid–air–liquid interface or 'Cassie–Baxter' state. The morphology of the coated substrate consists of randomly distributed corpuscular microstructures which encapsulate a film of trapped air (or 'plastron') upon contact with liquid. The reduction in viscous skin friction due to the plastron is evaluated using torque measurements in a parallel plate rheometer resulting in a measured slip length of $b_{slip} \approx 39$ μm, comparable to the mean periodicity of the microstructure evaluated from confocal fluorescence microscopy. The introduction of a large primary length-scale using dual-textured spray-coated meshes increases the magnitude of the effective slip length to values in the range 94 μm $\leq b_{slip} \leq$ 213 μm depending on the geometric features of the mesh. The wetted solid fractions on each mesh are calculated from free surface simulations on model sinusoidal mesh geometries. The trend in measured values of b_{slip} with the mesh periodicity L and the computed wetted solid-fraction $r\phi_s$ are found to be consistent with existing analytic predictions.

Received 12th February 2013
Accepted 28th March 2013

DOI: 10.1039/c3sm50445j

www.rsc.org/softmatter

1 Introduction

The local shearing flow of Newtonian fluids close to a solid surface is described by the Navier–Stokes equation along with an appropriate boundary condition on the velocity field at the liquid–solid interface. In macroscopic flows past smooth surfaces, where the length scale of the system is much larger than the molecular length scale, the adoption of the no-slip boundary condition is widely accepted as valid.[1] A more general condition used in various experimental studies investigating slip at molecular length scales is the Navier-slip hypothesis, $V_w = \beta\tau_w$, where V_w is the effective tangential surface velocity at the wall and τ_w is the local tangential shear-stress at the interface. For a Newtonian fluid whose viscosity is η, this expression can also be written in the form $V_w = b_{slip}\dot{\gamma}_w$, where $\dot{\gamma}_w = (dV/dz)_w$ is the local shear rate in the vicinity of the wall, and b_{slip} is the local slip length, a material property of the surface.[1–3] Physically, the slip length corresponds to the distance below the surface at which a linear extrapolation of the velocity profile would satisfy the no-slip boundary condition.[4,5] Multiple studies have investigated liquid-slip phenomena on smooth surfaces coated with low surface energy materials for which the molecular interactions at the solid–liquid interface become weak.[6–10] Although these investigations demonstrate that the no-slip boundary condition is not strictly valid, the resulting slip lengths across the solid–liquid interface are generally too small ($b_{slip} \approx$ 1–10 nm) to affect the macroscopic liquid flow significantly.

A growing body of work has attempted to utilize 'superhydrophobic' textured surfaces with regular microfabricated patterns or hierarchical textures[11–21] to amplify the effective fluid slip at the interface. On such non-wetting surfaces, the liquid layer sits on a composite solid–air interface (or Cassie–Baxter interface[22,23]), by entrapping pockets of air between the individual topographical features. The composite interface can robustly resist pressure-induced wetting transitions over a range of liquid surface tensions and externally imposed pressure differences by careful design of the fabricated surface morphology.[24,25] In facilitating the establishment of an air layer or 'plastron' that is stable to externally imposed pressure differences, such surfaces can reduce the frictional dissipation associated with laminar flows in microfluidic devices,[17,26] in rheometers,[20,27–29] in pipes,[21,30] over coated spheres[31] and in turbulent flows in channels.[32] The reduction in viscous skin friction due to the composite micro-textured interface can be significant in confined flows; in a seminal study, Watanabe *et al.* demonstrated a 14% reduction of drag in a 16 mm diameter pipeline textured with a superhydrophobic surface.[21] The vast

[a]Department of Chemical Engineering, Massachusetts Institute of Technology, Cambridge, MA, USA. E-mail: recohen@mit.edu

[b]Department of Mechanical Engineering, University of Texas at Dallas, USA

[c]Department of Mechanical Engineering, Massachusetts Institute of Technology, Cambridge, MA, USA. E-mail: gareth@mit.edu

† Electronic supplementary information (ESI) available: Viscosity and torque measurements of *n*-decane calibration liquid, side view of pinned liquid meniscus, array of confocal microscopy images at various depths, schematic of imaging setup, dynamic force trace of spray-coated mesh from tensiometry. See DOI: 10.1039/c3sm50445j

majority of subsequent investigations on superhydrophobic surfaces have involved precisely fabricated and regularly patterned geometries which help develop a systematic understanding of the influence of the wetted solid-fraction and surface periodicity in promoting large effective slip lengths and associated friction reduction. It is less clear whether substrates with randomly deposited micro-structures, which are cost-effective to manufacture and more readily applicable to large coated areas, would exhibit similar dramatic reduction in drag.[5,33] Sbragaglia and Prosperetti[34] and Feuillebois *et al.*[35] propose theoretical models to investigate how random textures can enhance the effective slip at a fluid–solid interface. In the present work, we use parallel-plate rheometery to determine the effective slip length for flow over spray-fabricated corpuscular microtextures that are randomly deposited over both flat substrates and on woven wire meshes.

In Fig. 1, we illustrate conceptually the effective slip present at the interface for flow over a spherically textured non-wetting substrate in the presence of an unconfined or pressure driven flow (Fig. 1a) and also in a laminar Couette flow (Fig. 1b). In each of these cases, the conventional no-slip condition is valid on the top of the wetted features, while the local fluid velocity at the liquid–air interface is determined by a tangential stress-balance. The net dissipative interaction of the fluid with this textured surface can be expressed using an area-averaged effective slip velocity $\langle V_w \rangle$, or alternatively in terms of an effective slip length $\langle b_{slip} \rangle$, again averaged over the periodicity (L) of the textured surface. As indicated in Fig. 1, the slip length $\langle b_{slip} \rangle$ can be greater than the characteristic scale of the texture ($2R$); a larger value of slip length indicates higher friction-reducing ability of the corresponding textured surface. For the laminar Couette flow shown in Fig. 1b, the velocity in the fluid varies linearly and the resulting shear rate $\dot{\gamma}$ is constant, except in the immediate vicinity of the surface texture. The apparent shear rate in the Couette flow (with the assumption of a no-slip boundary) $\dot{\gamma}_a = V_{plate}/h$ can be related to the true shear rate $\dot{\gamma}_t$ that is established in the fluid in the presence of slip as $\dot{\gamma}_a h = \dot{\gamma}_t(h + \langle b_{slip} \rangle)$, where h is the gap height.[36] For a Newtonian liquid with viscosity η and shear stress $\tau = \eta\dot{\gamma}$, measurement of the frictional forces or torques (in a torsional rheometer) due to Couette flow at a fixed height between two flat parallel rigid surfaces (with no slip) and textured non-wetting surfaces (with slip) enables the effective slip length on the latter to be directly related to the measured viscous friction using a rheometer.[20,27,28] The viscous stress for a linear Couette flow in the proximity of the top plate can be expressed as $\tau_{slip} = \eta V_{plate}(h + \langle b_{slip} \rangle)^{-1} = \eta\dot{\gamma}_a(1 + \langle b_{slip} \rangle/h)^{-1}$, where V_{plate} is the velocity of the upper plate. In a parallel-plate rheometer with disc radius R, the total torque $M = \int 2\pi r^2 \tau dr$ measured by the instrument for a Newtonian fluid is[37] $M = (\pi\eta\dot{\gamma}_a R^3)/2$. Therefore, for a fixed upper plate velocity, the ratio of the apparent viscosities (or measured torques) between (i) two flat surfaces with no slip and (ii) a flat surface and a textured non-wetting surface with slip can be directly related to the average slip as,

$$\frac{\eta_{flat}}{\eta_{slip}} = \frac{\tau_{flat}}{\tau_{slip}} = \frac{M_{flat}}{M_{slip}} = 1 + \frac{\langle b_{slip} \rangle}{h} \quad (1)$$

Eqn (1) implies that in order for fluid slip in confined laminar flows to be manifested as a significant effect, the magnitude of the slip length $\langle b_{slip} \rangle$ should be comparable to the length scale of the flow h (*i.e.*, $b/h \sim O(1)$). This can be readily achieved in a rheometer because gaps in the range $h \lesssim O(100$ μm) can be attained reliably.[38] A more universal measure of fluid slip is the fractional extent of drag reduction (DR) associated with the reduction in the measured apparent viscosities and can thus be written for a torsional Couette flow as:

$$DR = 1 - \frac{\eta_{slip}}{\eta_{flat}} = \frac{b_{slip}}{h + b_{slip}} \quad (2)$$

Rheometric torque measurements can therefore be usefully employed as a macroscopic measurement technique that provides a systematic method to probe area-averaged microscopic liquid-slip phenomenon over a large, random (and possibly anisotropic) surface morphology. Care must however be taken to ensure that edge effects are eliminated and systematic errors are minimized.[27,39,40]

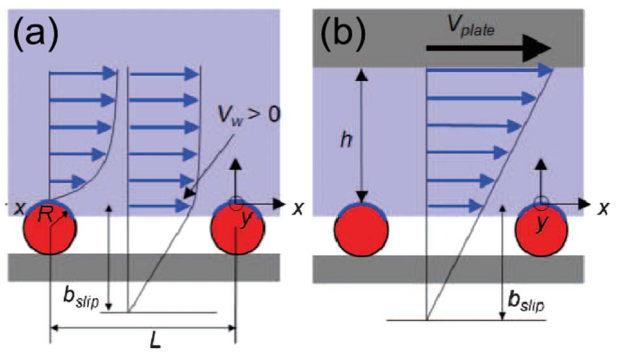

Fig. 1 (a) A schematic diagram showing a liquid flow on a textured non-wetting surface, possessing an effective velocity $\langle \bar{V}_w \rangle$ that is averaged over the texture period L. (b) A laminar Couette flow with average shear rate $\dot{\gamma}_a = V_{plate}/h$ between a non-wetting textured bottom surface exhibiting an average slip length $\langle b_{slip} \rangle$ and a conventional flat solid top surface possessing a no-slip boundary condition.

1.1 Relationship between slip length and surface textural parameters

The dependence of the effective slip length on the topographic properties of non-wetting textured surfaces has been analytically modeled using two limiting scenarios; (i) flow over a plastron of finite and constant thickness, and (ii) flow over surfaces with alternating regions of slip and no-slip. In the former case, for a liquid slipping over a homogeneous layer of air with thickness δ, the slip length is expressed as a product of the ratio of the viscosities η_{liquid}/η_{air} and a function of the plastron thickness.[19,31] McHale *et al.*[31] show that up to 30% drag reduction can be achieved for plastron-supporting spheres at the optimal plastron thickness. In the latter case, typical values of slip length on micro-textured non-wetting surfaces are on the order of tens of micrometers[13,29,41] and are dependent on the morphological patterning of the surface texture.[12,17] The topographical features needed to entrap microscopic air pockets at

the textured surface also act as regions where the conventional no-slip boundary condition still applies for each of the solid–liquid interfaces formed on the texture elements (blue solid lines in Fig. 1b). Therefore, the average value of the effective slip length becomes strongly dependent both on the fraction of the wetted solid–liquid interface (denoted generically as $r\phi_s$; the product of a roughness r and a projected area fraction of wetted solid ϕ_s)[42,43] and the size of the regions of slip and no-slip,[4,44] as well as the specific geometric arrangement of these regions.[45,46] For discrete textures such as periodically arrayed pillars or beads, a generic scaling law was developed by Ybert *et al.*[47] that predicts that the slip length scales as $\langle b_{slip}\rangle \sim a/(r\phi_s)$ in the limit $r\phi_s \to 0$, where a is the length scale corresponding to the size of individual surface features. The scaling law can also be expressed in terms of the periodicity L of the surface texture as $\langle b_{slip}\rangle \sim L\log(1/(r\phi_s))$ for 1D stripes and $\langle b_{slip}\rangle \sim L/\sqrt{r\phi_s}$ for 2D posts.[48] The validity of this model was demonstrated by numerical simulations and later by experiments with micro-fabricated surfaces.[14] The scaling law is also consistent with a number of studies that obtain analytical solutions of slip lengths for flow over 1D grooved and striped geometries.[4,48,49] Recent work by Ng and Wang[50] and Lauga and Davis[51] in solving for slip flow over micro-structures comprising periodic 2D circular posts also obtains an inverse square root dependence of the slip length with the solid fraction $b_{slip} \sim L/\sqrt{r\phi_s}$. In the present work, we use fluorescence microscopy and contact-angle measurements to obtain estimates of the mean periodicity $\langle L\rangle$ and the wetted area fraction $r\phi_s$ of a random microtexture in order to compare predictions from these theoretical models to the slip lengths obtained experimentally from rheometry.

2 Materials and methods

2.1 Single step fabrication of large area spray-coated non-wetting surfaces

A mixture of 50/50 wt% poly(methyl methacrylate) (Sigma–Aldrich; $M_w = 102\,000$ g mol^{-1}; PDI = 1.56) and the hydrophobic molecule 1*H*,1*H*,2*H*,2*H*-heptadecafluorodecyl polyhedral oligomeric silsesquioxane (fluorodecyl POSS), whose method of synthesis has previously been reported,[52] was dissolved in the commercially available solvent Asahiklin AK-225 at a concentration of 50 mg ml^{-1}. The mixture was subsequently spray-coated[53] onto circular silicon disks using an airbrush connected to a pressurized nitrogen stream at a distance of 20 cm and an operating pressure of 170 kPa. In Fig. 2a, we show a scanning electron micrograph of the micro-structure produced by jet break-up of the polymer solution during the spraying process. As seen from Fig. 2a, the surface structure consists of randomly deposited corpuscular beads of characteristic diameter ~20 μm. The nonvolatile PMMA acts as a sticky binder that adheres to the silicon surface. The presence of the hydrophobic fluorodecyl POSS molecules along with the re-entrant micro-structured morphology confers the textured and fluorine-rich surface with super non-wetting behaviour, which we have characterized in previous work.[53] In the inset of Fig. 2a, we show a drop of water of volume ~5 μl deposited on the spray-coated substrate. The drop exhibits an apparent advancing contact angle of $\theta^* = 161°$ and no observable hysteresis.

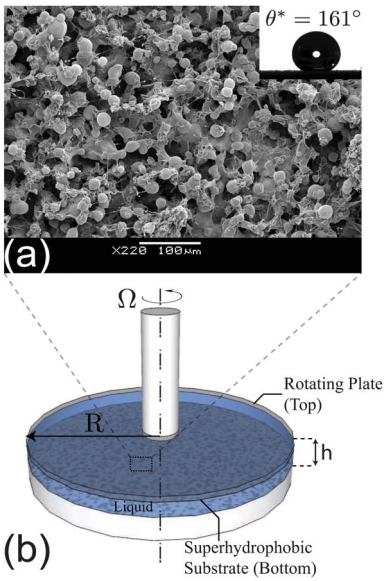

Fig. 2 (a) SEM image of spray-coated superhydrophobic surface displaying corpuscular micro-structured morphology. (b) Schematic of plate–plate fixture mounted on a controlled stress rheometer used to quantify apparent slip lengths using a 50 vol% glycerol–water mixture as probe liquid.

A water immersion test was performed to test the robustness against a pressure-induced wetting transition to the Wenzel state, and the spray-coated substrate remained in the composite or Cassie–Baxter state, as evidenced by the continued presence of the plastron, through the entire height of the water column (45 cm), which corresponds to a pressure of 4410 Pa. A number of woven metal meshes with various topography and characteristic length scales were also purchased from McMaster-Carr and conformally spray-coated with the 50 wt% PMMA–fluorodecyl POSS solution to produce hierarchical or dual length scale textures.

2.2 Rheometeric quantification of drag reduction and the slip length

An AR-G2 rheometer (TA instruments, New Castle, DE 19720) with a standard plate–plate geometry as shown in Fig. 2b was utilized to impose a shear rate and measure the resulting viscous torque on the samples. Eqn (1) is then used to calculate the resulting average slip lengths. A transparent upper acrylic plate of 60 mm diameter was used for all measurements. The spray-coated silicon substrates were affixed firmly to the lower Peltier plate using double-sided adhesive tape, and the upper plate was lowered to set the zero-gap height and ensure parallelism. Conventional rotational rheometers become prone to alignment errors in correctly zeroing the gap when very narrow fluid gaps are employed.[38] The mean error in gap height during calibration due to the plate–plate configuration was previously determined as 35 μm, although the non-flatness of the textured spray-coated substrate and the squeeze flow of air can contribute to an additional error.[54,55] To minimize contributions from these errors, a series of measurements were made at various gaps, from h = 500 μm to 2500 μm. After the zero-gap calibration is complete, rotational mapping was carried out to

account for residual system torques in the rheometer. Tests were performed at shear rates ranging between $10 \leq \dot{\gamma} \leq 100$ s^{-1}, unless specified otherwise.

2.3 Parameters influencing the rheometric measurement of effective slip length

There has been some discussion in the literature about the experimental reliability of obtaining accurate measurements of slip lengths *via* rheometry[39] as there are potential sources of systematic experimental error in the resolution of torque measurements, determining the gap height, presence of secondary flows and meniscus effects which need to be carefully accounted for.[40] As shown in the ESI (Fig. S1),† a reference Newtonian oil (*n*-decane; 25 °C; $\eta = 0.8538$ mPa s) was used for instrument calibration to obtain measurements of torques which yielded an experimental apparent viscosity of $\eta = 0.85 \pm 0.01$ mPa s for flow over a flat surface. The apparent viscosity was observed to be uniform over shear rates from $\dot{\gamma} = 10$–100 s^{-1} as expected, with the corresponding torques ranging between 0.3 and 1.3 μN m. While the torque resolution of the ARG2 rheometer in steady shear is stated to be 10 nN m,[56] scatter due to noise in the torque measurements was observed to be $\delta M \approx 0.2$ μN m. To amplify the magnitude of torque values, we use a 50 vol% glycerol–water as the Newtonian probe liquid with a measured viscosity of 6.2 ± 0.05 mPa s at 25°. The values of measured torques ranged from 3–30 μN m for shear rates between $\dot{\gamma} = 10$–100 s (as shown in ESI Fig. S1†). The choice of a 50 vol% glycerol–water as the probe liquid ensures that the range of measured torques M is much larger than the practical torque resolution limit of 0.2 μN m. The uncertainty in torque measurement is thus 0.7% at a shear rate of 100 s. The effects of inertia and secondary flow are negligible over the range of shear rates used.[57] Bocquet *et al.*[39] draw attention to an important source of systematic bias in the measured torque in parallel-plate rheometry on superhydrophobic surfaces due to the curvature of the liquid meniscus at the radial edge of the parallel plate, which can erroneously be interpreted as slip. The curvature of the free surface of the liquid filling the gap between the plates depends on the local contact angle of the fluid at the radial edges of the test fixtures and gives rise to a mismatch in the wetted area of the upper and lower fixtures. The decrease in the wetted radius is amplified on the spray-coated superhydrophobic substrate which exhibits an effective contact angle of $\theta^* \simeq 160°$. As described in ESI Fig. S2,† we introduce a thin hydrophilic circular strip of thickness 200 μm at a radius $R = 30$ mm in order to pin the liquid meniscus at the edge of the parallel plate. The reference torque measurements are performed on flat rigid surfaces with an advancing contact angle of $\theta^* = 90°$ obtained by spin-coating a silicon wafer with a 5/95% weight fraction fluorodecyl POSS–PMMA solution. This ensures that the area wetted by the liquid on the lower superhydrophobic surface is identical to that on the flat surface, minimizing the error associated with the edge effect. Furthermore, instead of using a single torque measurement to determine the effective slip length, a series of measurements were performed at a number of different gap heights, and the slip length was estimated from a least-squares fit of eqn (1) to reduce the effect of zero-gap errors.

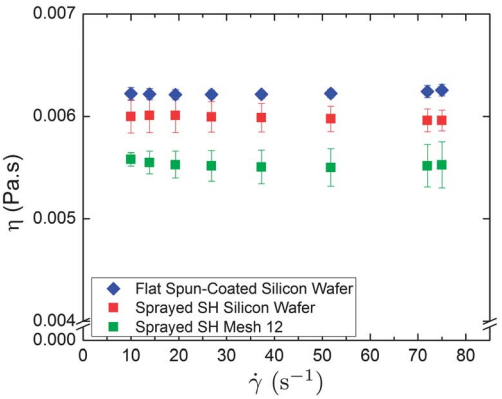

Fig. 3 Apparent viscosities of 50 vol% glycerol–water mixture measured for a gap separation of $h = 1000$ μm on (i) flat spin-coated hydrophobic surface; (ii) spray-coated superhydrophobic silicon wafer; (iii) spray-coated superhydrophobic mesh with wire radius $R = 254$ μm and mesh spacing $D = 805$ μm.

3 Results and discussions

In Fig. 3, we show the apparent viscosities of a 50 vol% glycerol–water solution measured at a fixed gap height of $h = 1000$ μm on three different surfaces. For this Newtonian fluid, the viscosity is rate independent and the mean value of the apparent viscosities are calculated as an average over the entire range of shear rates tested. For a flat spin-coated silicon wafer, the averaged viscosity was measured as $\bar{\eta}_{flat} = 6.2 \pm 0.05$ mPa s, which corresponds to the situation when there is no fluid slip. The averaged apparent viscosity for the spray-coated superhydrophobic corpuscular substrate shown in Fig. 2a is $\bar{\eta}_{slip} = 6.0 \pm 0.15$ mPa s corresponding to 3% reduction in the viscous drag and a spray-coated superhydrophobic woven mesh has an averaged apparent viscosity of $\bar{\eta}_{slip}^{mesh} = 5.5 \pm 0.14$ mPa s corresponding to a 11% reduction in drag at a gap height of $h = 1000$ μm. The lower values of the apparent viscosities on the spray-coated substrates is indicative of a reduction in drag due to partial fluid slip at the composite interface. However, as noted above it is not prudent to use measurements at a single height for the rheometric estimation of the slip length as uncertainties in zeroing the gap height and meniscus edge effects can be misinterpreted as contributions to the total slip. To minimize potential artifacts in the estimation of the effective slip length, measurements of the ratio of apparent viscosities on the flat substrate to that of the spray-coated substrate $y^{(i)} = (\bar{\eta}_{flat}/\bar{\eta}_{slip})^{(i)}$ (averaged over a range of shear rates as per Fig. 3) were repeated at various gap separations $h^{(i)}$. Linear regression of eqn (1) to values of $y^{(i)}$ for different values of $x^{(i)} = 1/h^{(i)}$ was then used to determine the best fit slope, which then yields the averaged effective slip length $\langle b_{slip} \rangle$.

3.1 Single-textured surfaces

In Fig. 4, we plot the ratio of $(\bar{\eta}_{flat}/\bar{\eta}_{slip})^{(i)}$ against the inverse gap height $1/h^{(i)}$ for the spray-coated silicon substrate with gap heights from $h^{(i)} = 500$ μm to $h^{(i)} = 2000$ μm in increments of 250 μm averaged over shear rates between 10 and 100 s. There are potentially a number of local wetting configurations of the

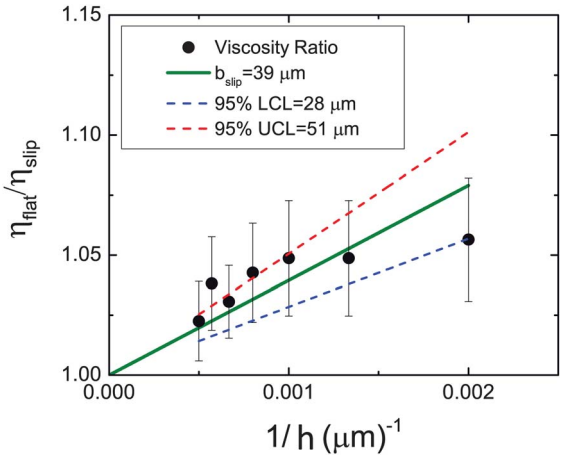

Fig. 4 Ratio of shear viscosity measured in contact with a flat surface to the apparent viscosity measured on the spray-coated superhydrophobic surface plotted against the inverse gap height. The effective slip length is extracted from a linear regression using eqn (1), and the corresponding 95% confidence bands are plotted as dashed lines.

composite interface upon each loading of the liquid in the parallel plate geometry, giving rise to variations in the measured apparent viscosity. The error bars correspond to experimental standard deviations over four sets of measurements at each gap height for the flat and sprayed-coated surfaces. Each data point at a particular gap height where $\bar{\eta}_{flat}/\bar{\eta}_{slip} > 1$ indicates the manifestation of effective slip, and a corresponding reduction in drag. A single parameter constrained best fit to the linear model in eqn (1) was performed and an instrumental weighting was used for the standard deviations (*i.e.*, the weighting function $w_i = 1/\sigma_i^2$), so that data points with larger deviations are assigned less importance. The mean value of the effective slip length for the spray-coated silicon substrate is $b_{slip} \approx 39$ μm with a 95% upper confidence limit of 51 μm and a 95% lower confidence limit of 28 μm. The corresponding confidence bands are plotted as dashed lines in Fig. 4. The extent of drag reduction observed is a function of the spacing between the plates as seen in eqn (2), and varies from 7% for a gap-height of 500 μm to 2% for a height of 2000 μm (2 mm).

The effective slip on randomly deposited textures is described by a tensorial quantity that varies depending on the local flow and the geometry specific to that local region.[45] Therefore, the numerical value of $\langle b_{slip} \rangle \approx 39$ μm we obtain from rheometry is a macroscopic averaged representation of the more complex velocity profiles that are established close to the rough hydrophobic texture shown in Fig. 2a. In order to understand the relationship between the mean spacing $\langle L \rangle$ of the beaded microstructures (Fig. 2a) and the values of $\langle b_{slip} \rangle$ obtained from torque measurements on our sprayed surface, we consider an equivalent periodic model geometry with the same wetted solid fraction as the sprayed substrate. It is convenient to use the Cassie–Baxter equation written in the form, $\cos \theta^* = r\phi_s \cos \theta_E - 1 + \phi_s$, to determine the wetted area fraction $r\phi_s$. Using a model of hexagonally packed spheres for the corpuscular structures, we have previously estimated[53] the total wetted fraction as $r\phi_s \approx 0.1$, where $\theta^* = 160^\circ$ is the macroscopic apparent contact angle on the sprayed substrate and $\theta_E = 124^\circ$ is the equilibrium contact angle on a flat spin-coated substrate with the same chemical composition as the POSS–PMMA mixture that is sprayed onto the substrate.

In order to use hydrodynamic models to evaluate the predicted slip present on a composite textured surface in which the wetted fraction is only $r\phi_s \simeq 10\%$ it is necessary to determine the characteristic length scale (denoted $\langle L \rangle$) of the random sprayed texture. We calculate the mean periodicity between the individual corpuscular features in Fig. 2b by incorporating fluorescent red dye (Nile red) in the fluorodecyl POSS–PMMA solution. The sample was then illuminated with a Helium/Neon (He/Ne) 543 nm laser, and the fluorescence was imaged using a Zeiss LSM 510 confocal microscope. The presence of the red dye, which is embedded in the microstructures produced on spraying, allows for mapping of the three-dimensional surface morphology (for details see ESI Fig. S3†). In Fig. 5, we show a 142 μm × 142 μm planar cross-section of the spray-coated corpuscular substrate imaged at a depth of 25 μm, which corresponds to the vertical midplane of the sprayed surface morphology. The confocal image was thresholded and converted to a binary image using the freely available ImageJ software package.[58] The light regions in Fig. 5 correspond to the voids between the corpuscular microstructure, and the dark regions indicate domains of fluorodecyl POSS–PMMA. The location of the centroids of each of these domains was determined by particle analysis, and the mean periodicity was obtained from the centroids using Delauney triangulation to be $\langle L \rangle \approx 32$ μm. The calculation of $\langle L \rangle$ and $r\phi_s$ for the spray-coated corpuscular morphology allows us to compare our experimentally measured slip length with analytical predictions that have been obtained for model periodic geometries. Ybert *et al.*[47] demonstrate that for a 2D array of solid patches in a square lattice, the slip length scales as:

$$\frac{b_{slip}}{L} = \frac{A}{\sqrt{r\phi_s}} - B \qquad (3)$$

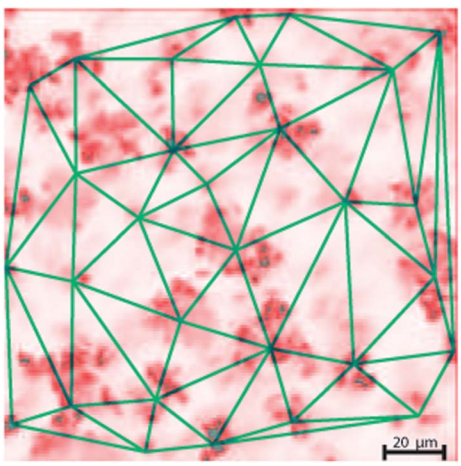

Fig. 5 Confocal microscope slice image of the spray-coated surface tagged with a red Nile dye and imaged at the mid-plane. The overlaid lines correspond to the Delaunay triangulation of the centroids of the individual microtextured features (determined from the ImageJ software), and is used to determine the mean periodicity $\langle L \rangle$.

where A and B are numerical constants that depend on the geometry of the patches. For periodic circular patches, the values of A and B are found by Ng and Wang[50] to be $A \approx 0.34$ and $B \approx 0.468$ using numerical regression, and by Lauga and Davis[51] as $A = 3\sqrt{\pi}/16 \approx 0.332$ and $B = 3\ln(1+\sqrt{2})/2\pi \approx 0.431$ using analytical methods. Substitution of $r\phi_s \approx 0.1$ and $\langle L \rangle \approx 32$ μm yields a predicted value of the slip length $b_{pred} \approx 19$ μm that is within a factor of two of our experimental result of $\langle b_{slip} \rangle \approx 39$ μm. The simple analytical model of an array of 2D circular patches is thus able to qualitatively predict the effective slip phenomenon measured near the spray-coated corpuscular micro-structures as a function of the mean periodicity $\langle L \rangle$ and the wetted fraction $r\phi_s$. Although the mean periodicity between the features of the corpuscular microstructure is limited by the operating parameters of the spray-coating system, we show in the next section that we can further enhance the effective slip by introduction of an additional length-scale *via* dual-textured mesh substrates.[15,59]

3.2 Dual textured non-wetting surfaces

Commercially woven wire meshes are readily available at comparatively low costs with a range of characteristic length scales and pore sizes. While most rigid metal meshes are hydrophilic, non-wetting hydrophobic meshes have been shown to support composite air–liquid interfaces[59,60] and are good candidate surfaces for reducing fluid drag. We use the spray-coating technique described earlier to deposit fluorodecyl POSS–PMMA microstructures onto various woven wire meshes, whose dimensions are summarized in Table 1. In Fig. 6a and b, we show scanning electron micrographs of a stainless steel mesh (Mesh II; $R = 127$ μm, $D = 330$ μm) that has been conformally spray-coated with the corpuscular microstructures. The spray-coated meshes exhibit superhydrophobic non-wetting behaviour and support a hierarchical composite air–liquid interface on two distinct scales: (i) on large scales of characteristic width $2D$ between the individual woven wires (of diameter $2R$) that comprise the mesh as shown in Fig. 6a and (ii) on smaller regions consisting of trapped air between the spray-coated corpuscular regions on the surface of the individual wires (shown in Fig. 6b) with a mean periodicity $\langle L_s \rangle \approx 32$ μm as discussed in the earlier section.

The reduction in the total wetted area fraction on this hierarchical structure is expected to further reduce the viscous friction. However, a number of factors, including the meniscus curvature, gravity, inertia, and other body forces, can give rise to a pressure difference that drives the liquid–air interface into the air pockets entrapped within the mesh.[24,61] The main source of external pressure in the plate–plate rheometer system is the Laplace pressure from the curvature of the meniscus as it sits on the wires. The Laplace pressure of the liquid sample in the rheometer is inversely related to the gap separation h as:

$$\Delta P = -\frac{2\gamma_{lv}\cos\theta}{h} \tag{4}$$

where $\theta = 160^\circ$ is the apparent contact angle on the micro-textured coating that has been applied on the wires of the mesh and γ_{lv} is the liquid surface tension. The magnitude of the applied pressure difference ΔP for the 50 vol% glycerol–water liquid varies from 64 Pa to 128 Pa for gap separations between 1000 μm and 2000 μm. The maximum pressure difference that can be supported across a liquid–air composite interface scales as $P_b \sim \gamma_{lv}/R_c$, where P_b is the breakthrough or impalement pressure and R_c is a characteristic length of the geometry.[43,62,63] For the dual-textured mesh, this characteristic length will scale with the mesh periodicity ($R_c \sim L = 2R + 2D$) for the larger air pockets trapped between the wires, and with the mean periodicity of the corpuscular microstructures ($R_c \sim \langle L \rangle$) for the smaller region on each wire. The large length scale of the mesh adversely affects its ability to maintain the pockets of air between the mesh wires against a pressure perturbation across the air film. For the cylindrically textured mesh surfaces used in this work, an approximate analytical expression for the breakthrough or impalement pressure was previously determined as:[25]

$$P_b = \frac{2\gamma_{lv}}{L}\left(\frac{2D^*}{D^*-1}\right)\left[\frac{(1-\cos\theta)}{(D^*-1+2\sin\theta)}\right] \tag{5}$$

The breakthrough pressure P_b is thus a function of the apparent contact angle θ, the characteristic length scale L and a dimensionless geometrical spacing ratio $D^* = (R + D)/R$. Therefore, as long as the external applied pressure difference $\Delta P < P_b$, the composite liquid–air interface is still stable and when $\Delta P \simeq P_b$, a wetting transition occurs in the large pockets of air trapped between the wires. The coated surface of the individual wires are themselves strongly non-wetting (*i.e.* $\theta = 160^\circ$) and continue to maintain their non-wetting characteristic (even after breakthrough in the large air pockets) due to the much smaller length scale of the microtextures formed by the spraying process.

In Fig. 6c, we show an image of the composite interface that is established upon depositing the glycerol–water probe liquid between the spray-coated mesh and a transparent upper plate. The image is obtained using a CCD camera focused through the upper plate of the rheometer at an oblique angle (for schematic, see ESI Fig. S4†). The dark regions in Fig. 6c correspond to the solid–liquid–air interface resting on the corpuscular structures that have been sprayed on the wires of the woven mesh, while the light regions correspond to incident light reflecting off the large pockets corresponding to the liquid–air interface. The position of the liquid–air interface depends on the externally applied pressure difference ΔP. A comparison between the composite interface that develops on the meshes in the plate–plate

Table 1 The Mesh number, radius of the individual wire (R), half-spacing between the wire meshes (D), the dimensionless spacing ratio $D^* = (R + D)/R$, the simulated wetted solid fraction ($r\phi_s$), robustness factor $A^* \approx P_b/P_{ref}$, experimental breakthrough pressure P_b, the effective slip length (b_{slip}) determined from experiments and the prediction from the model of Davis and Lauga (b_{mesh}, discussed in the main text, see eqn (7)) on the spray-coated woven meshes used in this work

Mesh	R (μm)	D (μm)	D^*	$r\phi_s$	A^*	P_b (Pa)	$\langle b_{slip} \rangle$ (μm)	b_{mesh} (μm)
I	70	229	4.3	0.17	4.99	190	92 ± 10	122
II	127	191	2.5	0.24	11.1	481	94 ± 7	108
III	127	326	3.6	0.25	4.4	180	157 ± 14	149
IV	254	452	2.8	0.40	4.1	112	194 ± 24	157
V	254	805	4.2	0.41	1.5	56	213 ± 15	219
VI	127	720	6.7	0.24	1.0	28	—	287

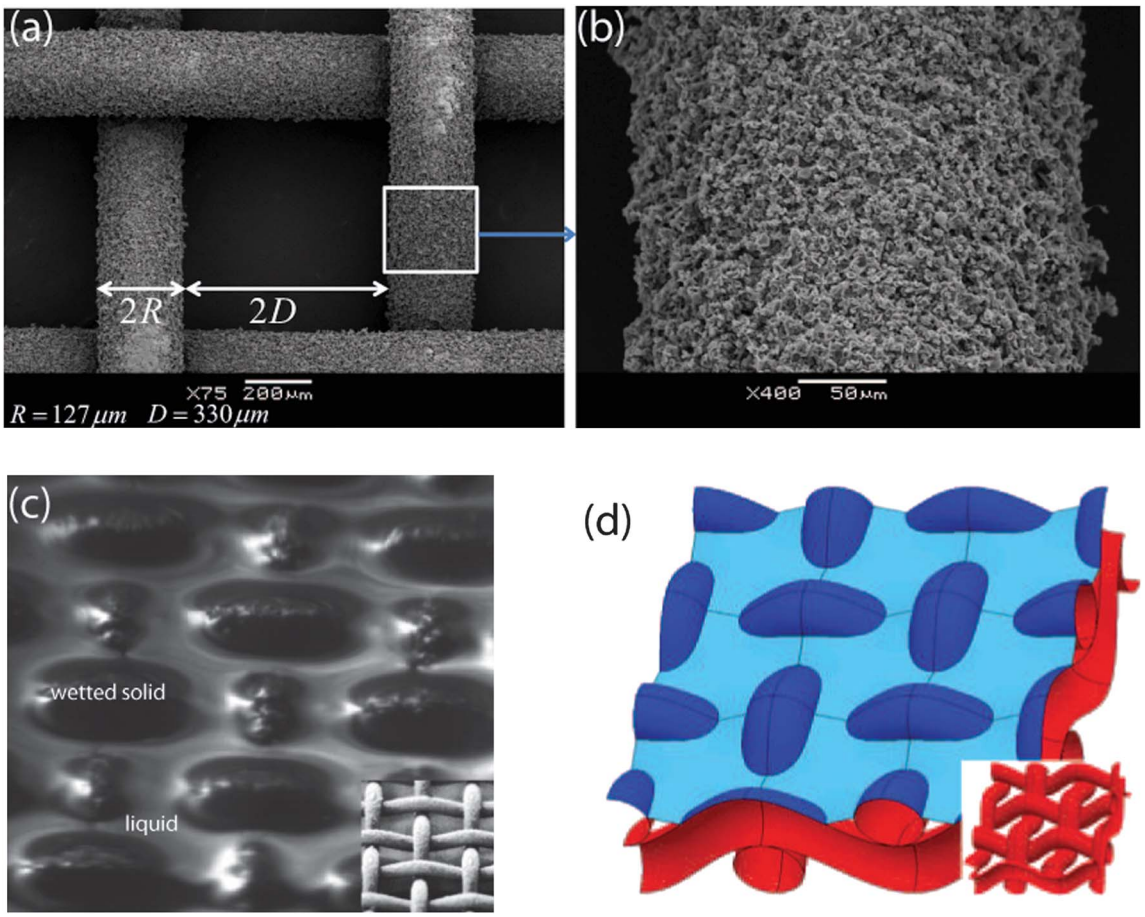

Fig. 6 (a and b) Scanning electron micrographs at different magnifications of the dual-textured spray-coated superhydrophobic mesh surfaces; (c) image of the solid–liquid–vapor composite interface for a 50 vol% glycerol–water solution resting between a spray-coated mesh and the upper rotating plate of the rheometer. The dark regions indicate the wetted area of the mesh and the light regions correspond to reflection of incident light off the liquid meniscus. The inset shows the structure of the spray-coated mesh in the dry state; (d) the composite interface on a model sinusoidal woven mesh, simulated using Surface Evolver FEM software. The dark blue, light blue, and red colors represent the wetted solid, liquid–air meniscus and the dry mesh surfaces respectively. The inset depicts the structure of the periodic mesh in the dry state.

rheometer and the simulated interface at a pressure differential of $\Delta P = 100$ Pa is provided in Fig. 6c and d. The meniscus configuration is calculated using the public domain Surface Evolver package.[64] The simulation captures the essential details of the composite interface system, including the wetted solid fraction $r\phi_s$ (dark blue) and the air–liquid fraction ϕ_a (light blue).

Such calculations can be combined with experimental measurements at different gap separations (and thus, from eqn (4), corresponding to different applied pressures) to understand the progressive decrease in the friction reduction that is achievable. Eqn (5) serves as a framework to allow for a rational selection of non-wetting meshes. The equation can be non-dimensionalized by a reference pressure $P_{ref} = 2\gamma_{lv}/l_{cap}$ (where $l_{cap} = \sqrt{\gamma_{lv}/\rho g}$ is the capillary length of the liquid) to obtain a dimensionless scaled breakthrough pressure $A^* = P_b/P_{ref}$. The reference pressure corresponds to the capillary pressure for a large drop of size l_{cap}, and is a measure of the pressure differential across a millimetric scale liquid droplet. Therefore, $A^* \lesssim 1$ is the appropriate criterion for the spontaneous wetting transition of the composite interface for a liquid drop on a freely suspended mesh. Six meshes with varying wire radii R and mesh spacing D satisfying $A^* \gtrsim 1$ were spray-coated and the breakthrough pressure P_b for each sprayed mesh was experimentally determined by vertical immersion into a 50 vol% glycerol–water solution using a dynamic tensiometer and analysis of the resultant force curves (see ESI Fig. S5†). In order to prevent an irreversible wetting transition during the rheometry experiments, the underlying flat surface on which the mesh was horizontally affixed was also spray-coated with the corpuscular microtexture to make it superhydrophobic. The experimentally measured values of P_b are shown in Table 1, along with the values of D^* and A^*. The measured breakthrough pressures are qualitatively consistent with the simple cylindrical model of eqn (5). As higher pressures are applied across the composite liquid–air interface, the liquid meniscus descends into the weave of the mesh until the meniscus between the wires collapses and rests on the bottom surface. Therefore, the numerical value of A^* can also be interpreted as a robustness factor, *i.e.*, a measure of the susceptibility of the meniscus to exhibit this sagging behaviour. Meshes with $A^* \gg 1$ are

robustly metastable, while meshes exhibiting $A^* \approx 1$ are more prone to a wetting transition.[24,25,63] The presence of the flat spray-coated bottom substrate and the connectivity of the air pockets allow the meniscus to reversibly recover to its original location upon removal of the pressure difference acting on the plastron.

Davis and Lauga[65] have analytically studied liquid flow along the principal direction of an ideal flat 2D continuous mesh substrate, and obtain an asymptotic estimate for the slip length in the limit of a widely spaced mesh of thin rungs ($D^* = (R + D)/R \gg 1$) as

$$b_{\text{ideal}} \approx \frac{L}{3\pi} \ln\left(\frac{2D^*}{\pi}\right) \tag{6}$$

where $L = 2R + 2D$ is the mesh periodicity. Eqn (5) and (6) clearly convey the inverse correlation between the magnitude of the slip length and the robustness of the composite interface. Any attempt to increase the slip length by increasing D^* and L will directly result in a reduction in the robustness of the composite interface. In Fig. 7, we illustrate this inverse correlation by means of an engineering design chart consisting of fixed contours of the robustness factor A^* (dashed lines) and the slip length (solid line) on an ideal mesh b_{ideal} (computed from eqn (5) and (6) respectively) plotted as a function of the mesh periodicity L and the spacing ratio D^*. The shaded portion indicates inaccessible regions of the design space (where $A^* < 1$, corresponding to a spontaneous wetting transition of the mesh from the Cassie–Baxter state to a Wenzel state). Fig. 7 provides a systematic framework with which to design the geometry of non-wetting meshes for reducing frictional drag, while clearly illustrating the difficulty of simultaneously achieving both large liquid slip lengths and high robustness. The various meshes used in this study are also indicated in Fig. 7 by points I–VI, and

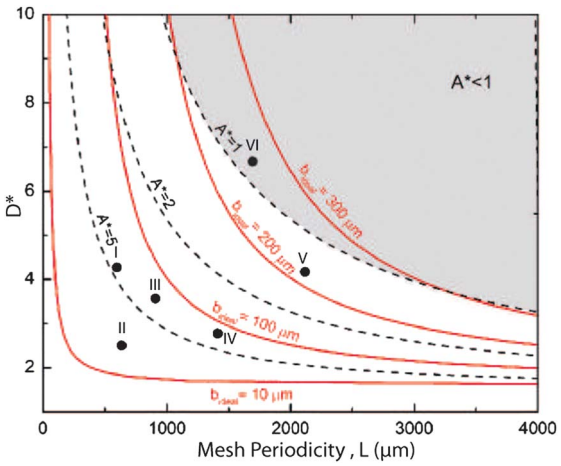

Fig. 7 The design chart for ideal flat non-wetting mesh surfaces, with contours of fixed slip length plotted as solid red lines (from eqn (6)) and contours of fixed robustness factor A^* drawn as dashed black lines as a function of the dimensionless spacing ratio $D^* = (R + D)/R$ and the mesh periodicity $L = 2D + 2R$. The shaded region indicates parts of the design space where $A^* < 1$ and the liquid meniscus will penetrate into the mesh. The data points correspond to the location in the design space of the various superhydrophobic coated meshes used in this study.

experiments to calculate their friction reducing characteristics are discussed in the following sections.

It is important to note that a number of assumptions in the ideal model system considered by Davis and Lauga are not strictly valid during parallel plate rheometry over the spray-coated mesh surfaces. These include the existence of a continuously connected solid–liquid wetted region, a flat liquid–air interface, and the uniform directionality of the imposed flow. Despite the continuous nature of the fibrous woven meshes shown in Fig. 6a, the real contact regions between the liquid and the textured solid surface consists of arrays of discrete elliptical wetted patches as shown in Fig. 6d. In order to calculate the expected frictional drag of these mesh surfaces it is necessary to evaluate the wetted surface fraction as it evolves with the imposed pressure. A set of simulations computing the deformation of the liquid–air interface on model sinusoidal woven meshes under imposed pressure differentials were performed using Surface Evolver. In Fig. 8a and b, we illustrate the computed shape of the composite liquid–air meniscus on Mesh II (with robustness factor $A^* = 11.1$) at pressure differentials of $\Delta P = 100$ Pa and $\Delta P = 500$ Pa respectively. The total wetted solid fraction calculated from the simulation increases from $r\phi_s = 0.24$ at $\Delta P = 100$ Pa to $r\phi_s = 0.78$ at $\Delta P = 500$ Pa. At a fixed pressure differential of $\Delta P = 100$ Pa, the wetted fraction $r\phi_s$ also depends on the geometry of the woven mesh. The more open Mesh IV (Fig. 8c) has a reduced robustness factor ($A^* = 4.1$), and consequently the liquid–air interface penetrates deeper into the mesh, corresponding to a larger wetted solid fraction of $r\phi_s = 0.40$. In Fig. 8d, we show the variation of the total liquid–solid wetted area fraction $r\phi_s$ and liquid–air area fraction ϕ_a with the imposed pressure differential ΔP. The woven topography of the meshes allows for the sum $r\phi_s + \phi_a > 1$ in general.[42,43] The liquid–air interface visibly distorts or 'sags' with increasing pressure differences, considerably increasing the wetted solid fraction $r\phi_s$ on the given texture and correspondingly weakening the overall friction reduction that can be expected. In Table 1, we present the wetted solid fractions on each mesh used in this study calculated at an intermediate pressure differential of $\Delta P = 100$ Pa.

On an ideal flat mesh (with $r = 1$), the wetted solid fraction $r\phi_s$ is directly related to the dimensionless geometrical spacing ratio as $D^* \equiv (R + D)/R = (1 + \sqrt{1 - r\phi_s})/r\phi_s$. While it is clearly evident from the surface evolver simulations that the model of a continuously connected flat mesh is not strictly correct for robustly non-wetting meshes, the simulated values of $r\phi_s$ can be used to obtain an alternative estimate for the slip length b_{mesh} on a woven texture by eliminating D^* from eqn (6) to obtain

$$b_{\text{mesh}} \approx \frac{L}{3\pi} \ln\left(\frac{2\left(1 + \sqrt{1 - r\phi_s}\right)}{\pi r\phi_s}\right) \tag{7}$$

Eqn (7) enables us to evaluate the expected value of the slip length that can be generated for the spray-coated woven meshes, where the value of $r\phi_s$ is estimated for a mesh of given geometrical dimensions using Surface Evolver as shown in Fig. 8. We present predictions of the effective slip length in Table 1 along with values obtained experimentally from rheometry.

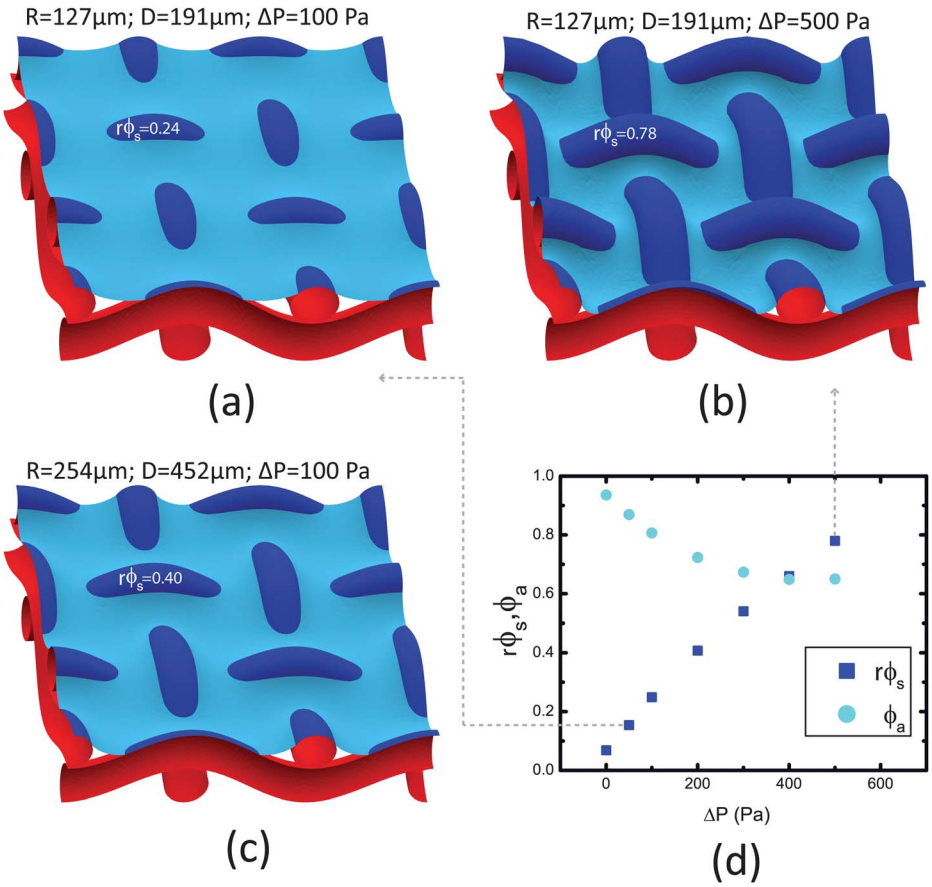

Fig. 8 The simulated composite interface and wetted solid fractions ($r\phi_s$) on sinusoidal woven wire meshes of diameter $R = 127$ μm and spacing $D = 191$ μm (corresponding to Mesh II), calculated using Surface Evolver at imposed pressure differentials of (a) $\Delta P = 100$ Pa resulting in $r\phi_s = 0.24$ and (b) $\Delta P = 500$ Pa resulting in $r\phi_s = 0.40$. (c) The simulated composite interface corresponding to Mesh IV ($R = 254$ μm; $D = 452$ μm) at $\Delta P = 100$ Pa with $r\phi_s = 0.40$; (d) the variation of the wetted solid fraction $r\phi_s$ and the air–liquid area fraction ϕ_a with increasing pressure differential (on Mesh II) arising from the Laplace pressure associated with decreasing plate–plate height ($\Delta P \propto 1/H$, see eqn (4)).

In Fig. 9, we plot the ratio of the averaged viscosity measured on a flat surface to that of the superhydrophobic mesh $\bar{\eta}_{flat}/\bar{\eta}_{mesh}$ against the inverse gap height $1/h$ for a series of four meshes. A linear least squares fit of eqn (1) was performed to determine the mean slip lengths which are shown in Table 1, along with the predicted slip lengths (eqn (7)) using the simulated wetted solid fractions calculated for each mesh. The dual textured meshes I to IV show a larger decrease in the apparent viscosity for a given height in the rheometer when compared to the sprayed corpuscular structures discussed in the first section. For a fixed wire radius $R = 127$ μm, the slip length is observed to increase with mesh spacing, from $\langle b_{slip} \rangle \approx 94$ μm for Mesh II ($D = 191$ μm) to $\langle b_{slip} \rangle \approx 157$ μm for Mesh III ($D = 326$ μm). Upon further increasing the mesh periodicity (Mesh V: $R = 254$, $D = 805$ μm, $A^* = 1.5$), the effective slip length increases to $\langle b_{slip} \rangle \approx 213$ μm but the mesh exhibits a lower robustness to the wetting transition. The measured slip lengths on these spray-coated meshes are consistent with the analytical prediction for b_{mesh} obtained from eqn (7). The effect of meniscus sagging is most evident for Mesh VI ($A^* = 1.0$), for which $\bar{\eta}_{flat}/\bar{\eta}_{mesh} < 1$ for $h \leq 1250$ μm signifying enhanced form drag when the liquid meniscus lies fully in between the features of the mesh. As shown in Fig. 9d, a systematic decrease in the ratio of viscosities corresponding to enhanced frictional dissipation is observed as the Laplace pressure drives the liquid further into the mesh features at lower gap heights.

The variation of the effective slip lengths of the different geometries depends on the periodicity of the mesh L and the wetted solid fractions *via* eqn (7). In Fig. 10, we plot the ratio of $\langle b_{slip} \rangle / L$ against values of the wetted solid fraction $r\phi_s$ (obtained from Surface Evolver simulations) for each of the meshes. The solid line corresponds to the prediction obtained from eqn (7) and the dashed line is an alternate estimate of the slip length from eqn (3) which approximates the ellipsoidal wetted regions as a series of discrete circular patches.[47,50] Despite the non-ideal topographic features of the woven mesh surface (*i.e.*, fabrication tolerances, waviness and form drag), the model of Davis and Lauga given by eqn (7) captures the slow variation of the experimentally obtained slip values with the wetted solid fraction (calculated from Surface Evolver simulations) over the range of woven meshes used in our study. We are able to generate maximum slip lengths of $\langle b_{slip} \rangle \simeq 213$ μm corresponding to a friction reduction of 30% for a gap of 500 μm on Mesh V. Our

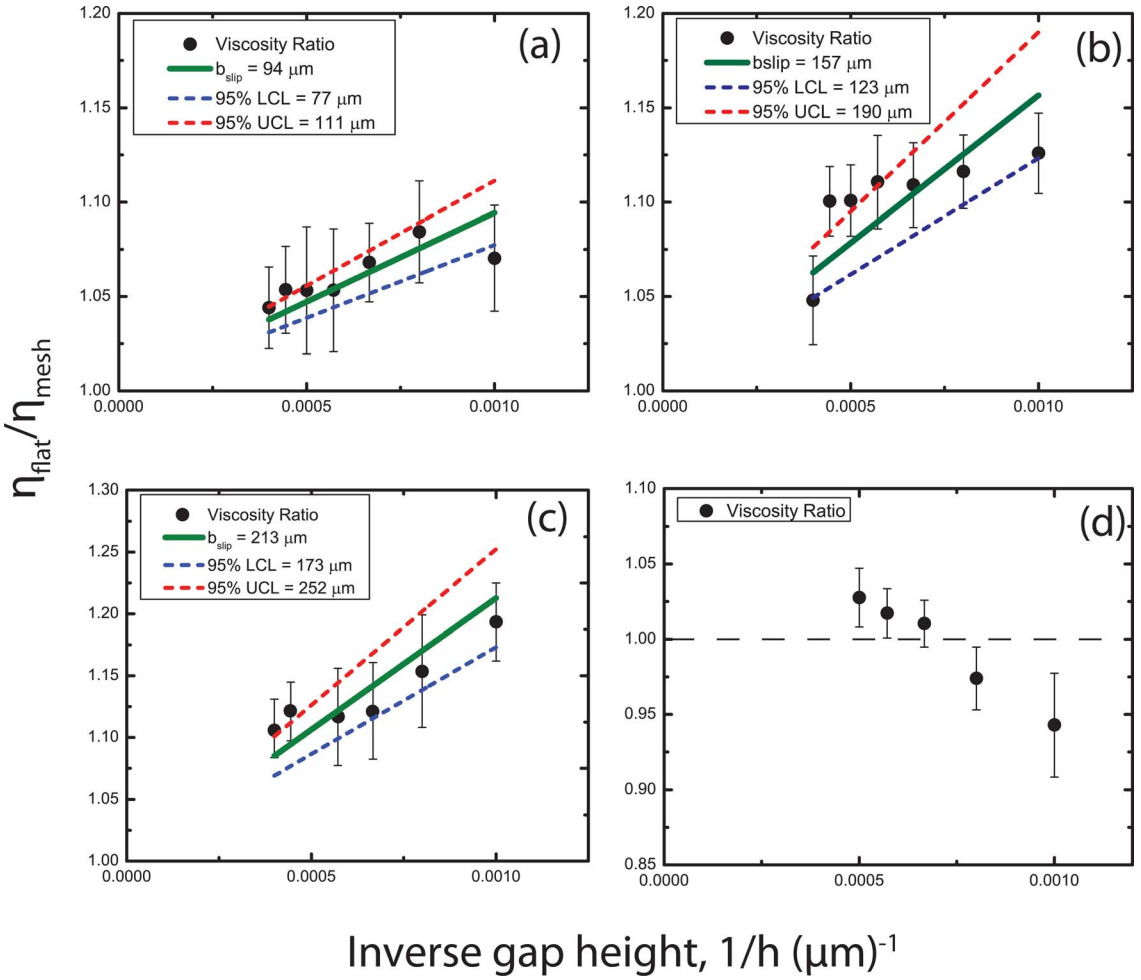

Fig. 9 Ratio of measured viscosity on a flat surface to the apparent viscosity measured on the friction reducing mesh plotted against the inverse gap height on the following spray-coated meshes surface: (a) Mesh II with $R = 127$ μm and $D = 191$ μm (b) Mesh III with $R = 127$ μm and $D = 326$ μm (c) Mesh V with $R = 254$ μm and $D = 805$ μm (d) Mesh VI with $R = 127$ μm and $D = 720$ μm. On the latter mesh, little or no friction reduction is observed due to a wetting transition; in fact the fully wetted Wenzel state results in an enhanced form drag. The slip lengths for each mesh were extracted from a linear regression to eqn (1), and the dotted lines on each plot correspond to the 95% confidence bands.

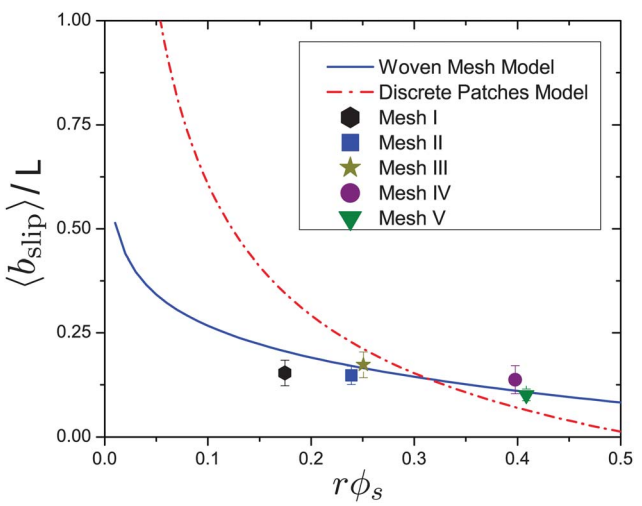

Fig. 10 Ratio of b_{slip}/L plotted against the solid area fraction $r\phi_s$ for Meshes I–V. The solid blue line and dashed red line correspond to the predictive curves for b_{mesh} (from eqn (7)) and $b_{discrete}$ (from eqn (3)) respectively.

results indicate that giant liquid slip can only be obtained as $r\phi_s \rightarrow 0$, consistent with the work of Lee and Kim[15] who study 2D post surfaces (with very low area fractions $\phi_s \approx 1\%$). These large slip lengths can be achieved with woven meshes by judicious choice of D^* and L, as well as by increasing the intrinsic non-wettability of the mesh coating (*i.e.* increasing the value of the contact angle θ_E). However, as we demonstrate in eqn (5) and Fig. 10, such an increase in the slip length necessitates a tradeoff in the robustness of the mesh against wetting transitions.

4 Conclusions

In this work, we have demonstrated the friction reducing characteristics of a spray-coated fluorodecyl POSS–PMMA superhydrophobic surface composed of randomly deposited corpuscular microstructures. The effective slip length on the spray-coated surface was determined from rheometric force measurements involving careful experimental design. Factors considered include radial pinning of the liquid meniscus at the

edge of the geometry, choice of operating shear rates and the use of multiple gap heights to address concerns over systematic errors such as edge effects and potential inaccuracies in torque measurement associated with this technique.[39,40] The effective slip length on the sprayed microstructures was obtained using a weighted linear least-squares fit as $\langle b_{slip} \rangle \approx 39$ μm with a 95% upper-confidence interval of 51 μm and a 95% lower-confidence interval of 28 μm with a reduction of drag ranging from 2–7% corresponding to gap heights between 2000 μm to 500 μm. The mean periodicity and wetted area fraction was determined from fluorescence microscopy and contact angle measurements as $\langle L \rangle \approx 32$ μm and $r\phi_s \approx 0.10$ respectively. The effective slip length was observed to be qualitatively consistent with that expected from a simple equivalent model of 2D periodic circular patches.

The larger intrinsic periodicity L in dual-scale sprayed superhydrophobic meshes can greatly increase the achievable slip length. We determined the effective slip length for a series of spray-coated meshes and the extracted effective slip length on the spray-coated meshes ranges between $\langle b_{slip} \rangle \approx 94$ μm to $\langle b_{slip} \rangle \approx 213$ μm (see Table 1). The slow variation of the slip length is consistent with the prediction of Davis and Lauga, with the wetted solid fraction $r\phi_s$ for each mesh determined from Surface Evolver simulations. By comparing the governing equations for the slip length with a dimensionless expression for robustness of the slip-inducing composite interface, we also have shown that the slip lengths of such composite interfaces have a strong inverse coupling with the robustness of the plastron film. This inverse correlation occurs because both the liquid slip and the robustness of the composite interface are scale-dependent properties, unlike static measures of superhydrophobicity such as the effective advancing contact angle θ^*. The simplicity of the solution spraying process used in the present study is particularly helpful in facilitating rapid and cheap production of friction-reducing coatings that can be applied over large areas. When combined with periodic textures (such as woven meshes or cylindrical post arrays) that can help support the composite vapour–liquid–solid interface (or plastron), very large slip lengths can be established.

Acknowledgements

We acknowledge financial support from the Army Research Office (ARO) through Contract W911NF-07-D-0004, the Office of Naval Research (ONR) through Contract 3002452814, as well as the Air Force Research Laboratory, Propulsion Directorate, Air Force Office of Scientific Research. We thank Prof. Michael F. Rubner and the Institute for Soldier Nanotechnologies at MIT for the use of various laboratory facilities, Jonathan Gilbert for assistance with confocal microscopy, Dr Adam Meuler, Dr Jonathan DeRocher, Justin Kleingartner and Hyomin Lee for helpful discussions during the preparation of this manuscript.

References

1 E. Lauga, M. Brenner and H. Stone, in *Microfluidics: The No-Slip Boundary Condition Springer Handbook of Experimental Fluid Mechanics*, ed. C. Tropea, A. L. Yarin and J. F. Foss, Springer Berlin Heidelberg, 2007, pp. 1219–1240.
2 P. G. de Gennes, *Langmuir*, 2002, **18**, 3413–3414.
3 J. P. Rothstein, *Annu. Rev. Fluid Mech.*, 2010, **42**, 89–109.
4 E. Lauga and H. A. Stone, *J. Fluid Mech.*, 2003, **489**, 55–77.
5 L. Bocquet and E. Lauga, *Nat. Mater.*, 2011, **10**, 334–337.
6 J. L. Barrat and L. Bocquet, *Phys. Rev. Lett.*, 1999, **82**, 4671–4674.
7 D. M. Huang, C. Sendner, D. Horinek, R. R. Netz and L. Bocquet, *Phys. Rev. Lett.*, 2008, **101**, 226101.
8 R. Pit, H. Hervet and L. Leger, *Phys. Rev. Lett.*, 2000, **85**, 980–983.
9 R. S. Voronov, D. V. Papavassiliou and L. L. Lee, *Ind. Eng. Chem. Res.*, 2008, **47**, 2455–2477.
10 D. C. Tretheway and C. D. Meinhart, *Phys. Fluids*, 2002, **14**, L9–L12.
11 L. Bocquet and J. L. Barrat, *Soft Matter*, 2007, **3**, 685–693.
12 C. H. Choi, U. Ulmanella, J. Kim, C. M. Ho and C. J. Kim, *Phys. Fluids*, 2006, **18**, 087105.
13 S. Gogte, P. Vorobieff, R. Truesdell, A. Mammoli, F. v. Swol, P. Shah and C. J. Brinker, *Phys. Fluids*, 2005, **17**, 051701.
14 C. Lee, C. H. Choi and C. J. Kim, *Phys. Rev. Lett.*, 2008, **101**(6), 64501.
15 C. Lee and C.-J. Kim, *Langmuir*, 2009, **25**, 12812–12818.
16 G. McHale, N. J. Shirtcliffe, C. R. Evans and M. I. Newton, *Appl. Phys. Lett.*, 2009, **94**, 064104.
17 J. Ou, B. Perot and J. P. Rothstein, *Phys. Fluids*, 2004, **16**, 4635–4643.
18 J. Ou and J. P. Rothstein, *Phys. Fluids*, 2005, **17**, 103606–103610.
19 D. C. Tretheway and C. D. Meinhart, *Phys. Fluids*, 2004, **16**, 1509–1515.
20 R. Truesdell, A. Mammoli, P. Vorobieff, F. van Swol and C. J. Brinker, *Phys. Rev. Lett.*, 2006, **97**, 044504.
21 K. Watanabe, Y. Udagawa and H. Udagawa, *J. Fluid Mech.*, 1999, **381**, 225–238.
22 A. Cassie and S. Baxter, *Trans. Faraday Soc.*, 1944, **40**, 546–551.
23 D. Quéré, *Annu. Rev. Mater. Res.*, 2008, **38**, 71–99.
24 A. Tuteja, W. Choi, M. L. Ma, J. M. Mabry, S. A. Mazzella, G. C. Rutledge, G. H. McKinley and R. E. Cohen, *Science*, 2007, **318**, 1618–1622.
25 S. S. Chhatre, W. Choi, A. Tuteja, K. C. Park, J. M. Mabry, G. H. McKinley and R. E. Cohen, *Langmuir*, 2010, **26**, 4027–4035.
26 C. F. Carlborg and W. van der Wijngaart, *Langmuir*, 2010, **27**, 487–493.
27 C. H. Choi and C. J. Kim, *Phys. Rev. Lett.*, 2006, **96**, 066001.
28 J. Li, M. Zhou, L. Cai, X. Ye and R. Yuan, *Chin. Sci. Bull.*, 2009, **54**, 4560–4565.
29 M. Zhou, J. Li, C. X. Wu, X. K. Zhou and L. Kai, *Soft Matter*, 2011, **7**, 4391–4396.
30 N. J. Shirtcliffe, G. McHale, M. I. Newton and Y. Zhang, *ACS Appl. Mater. Interfaces*, 2009, **1**, 1316–1323.
31 G. McHale, M. R. Flynn and M. I. Newton, *Soft Matter*, 2011, **7**, 10100–10107.
32 R. J. Daniello, N. E. Waterhouse and J. P. Rothstein, *Phys. Fluids*, 2009, **21**, 085103–085112.

33 M. A. Samaha, H. V. Tafreshi and M. Gad-el Hak, *Phys. Fluids*, 2011, **23**, 012001–012008.
34 M. Sbragaglia and A. Prosperetti, *J. Fluid Mech.*, 2007, **578**, 435–451.
35 F. Feuillebois, M. Z. Bazant and O. I. Vinogradova, *Phys. Rev. Lett.*, 2009, **102**, 026001.
36 A. Yoshimura and R. K. Prud'homme, *J. Rheol.*, 1988, **32**, 53–67.
37 R. B. Bird, R. C. Armstrong and O. Hassager, Dynamics of Polymeric Liquids, *Fluid Mechanics*, 2nd edn, 1987, vol. 1.
38 C. J. Pipe, T. S. Majmudar and G. H. McKinley, *Rheol. Acta*, 2008, **47**, 621–642.
39 L. Bocquet, P. Tabeling and S. Manneville, *Phys. Rev. Lett.*, 2006, **97**, 109601.
40 C. H. Choi and C. J. Kim, *Phys. Rev. Lett.*, 2006, **97**, 109602.
41 C. Lee and C.-J. Kim, *Phys. Rev. Lett.*, 2011, **106**, 014502.
42 A. J. B. Milne and A. Amirfazli, *Adv. Colloid Interface Sci.*, 2012, **170**, 48–55.
43 H.-J. Butt, C. Semprebon, P. Papadopoulos, D. Vollmer, M. Brinkmann and M. Ciccotti, *Soft Matter*, 2013, **9**, 418–428.
44 J. R. Philip, *Z. Angew. Math. Phys.*, 1972, **23**, 353–372.
45 K. Kamrin, M. Z. Bazant and H. A. Stone, *J. Fluid Mech.*, 2010, **658**, 409–437.
46 I. V. Olga and V. B. Aleksey, *J. Phys.: Condens. Matter*, 2011, **23**, 184104.
47 C. Ybert, C. Barentin, C. Cottin-Bizonne, P. Joseph and L. Bocquet, *Phys. Fluids*, 2007, **19**, 123601–123610.
48 C.-O. Ng and C. Y. Wang, *Phys. Fluids*, 2009, **21**, 013602.
49 C. Cottin-Bizonne, C. Barentin, E. Charlaix, L. Bocquet and J. L. Barrat, *Eur. Phys. J. E: Soft Matter Biol. Phys.*, 2004, **15**, 427–438.
50 C.-O. Ng and C. Wang, *Microfluid. Nanofluid.*, 2010, **8**, 361–371.
51 A. M. J. Davis and E. Lauga, *J. Fluid Mech.*, 2010, **661**, 402–411.
52 J. M. Mabry, A. Vij, S. Iacono and B. Viers, *Angew. Chem., Int. Ed.*, 2008, **47**, 4137–4140.
53 S. Srinivasan, S. S. Chhatre, J. M. Mabry, R. E. Cohen and G. H. McKinley, *Polymer*, 2011, **52**, 3209–3218.
54 C. Clasen, B. P. Gearing and G. H. McKinley, *J. Rheol.*, 2006, **50**, 883–905.
55 G. A. Davies and J. R. Stokes, *J. Rheol.*, 2005, **49**, 919–922.
56 B. Costello, *The AR-G2 Magnetic Bearing Rheometer*, http://www.tainstruments.co.jp/application/pdf/Rheology_Library/Application_Briefs/RH085.pdf.
57 C. Macosko, *Rheology: Principles, Measurements, and Applications*, Wiley-VCH, 1994.
58 M. Abramoff, P. Magalhaes and S. Ram, *Biophotonics International*, 2004, **11**, 36–42.
59 T. An, S. J. Cho, W. Choi, J. H. Kim, S. T. Lim and G. Lim, *Soft Matter*, 2011, **7**, 9867–9870.
60 L. Feng, Z. Zhang, Z. Mai, Y. Ma, B. Liu, L. Jiang and D. Zhu, *Angew. Chem., Int. Ed.*, 2004, **43**, 2012–2014.
61 D. Quéré and M. Reyssat, *Philos. Trans. R. Soc., A*, 2008, **366**, 1539–1556.
62 M. Reyssat, J. M. Yeomans and D. Quéré, *Europhys. Lett.*, 2008, **81**, 26006.
63 A. Tuteja, W. Choi, J. M. Mabry, G. H. McKinley and R. E. Cohen, *Proc. Natl. Acad. Sci. U. S. A.*, 2008, **105**, 18200–18205.
64 K. A. Brakke, *Philos. Trans. R. Soc., A*, 1996, **354**, 2143–2157.
65 A. M. J. Davis and E. Lauga, *Phys. Fluids*, 2009, **21**, 113101.

